ZnO/Cu₂O heterojunction integrated fiber-optic biosensor for remote detection of cysteine

Xingyue Wen[a], Xinyu Chang[a], Aohua Li[a], Xinghua Yang[a,*], Fengjun Tian[a], Zhihai Liu[a], Nigel Copner[b],

Pingping Teng[a,*], Libo Yuan[a,c]

[a]Key Laboratory of In-Fiber Integrated Optics, Ministry of Education, College of Physics and

Optoelectronic Engineering, Harbin Engineering University, Harbin 150001, China

[b]Wireless & Optoelectronics Research & Innovation Centre, Faculty of Computing, Engineering &

Science, University of South Wales, Wales, CF37 1DL, UK

[c]Photonics Research Center, Guilin University of Electronics Technology, Guilin 541004, China

Fax: 0086-451-82519850

Phone: 0086-451-82519850

E-mail:[*] yangxh@hrbeu.edu.cn; tengpingping@hrbeu.edu.cn

Abstract

Indium tin oxide, semiconductor nanomaterial ZnO, and Cu_2O were first loaded on the surface of the optical fiber to form an optical fiber probe. Large-volume macroscopic spatial light is replaced by an optical fiber path, and remote light injection is implemented. Based on the optical fiber probe, a photoelectrochemical biosensor was constructed and remote detection of cysteine was realized. In this tiny device, the optical fiber probe not only acts as a working electrode to react with the analyte but also directs the light exactly where it is needed. Simultaneously, the electrochemical behavior of cysteine on the surface of the working electrode is dominated by diffusion-control, which provides strong support for quantitative detection. Then, under the bias potential of 0 V, the linear range of the fiber-optic-based cysteine biosensor was 0.01~1 μM, the regression coefficient (R^2) value was 0.9943. In spiked synthetic urine, the detection of cysteine was also realized by the integrated biosensor. Moreover, benefiting from the low optical fiber loss, the new structure also possesses a unique remote detection function. This work confirms that photoelectrochemical biosensors can be integrated via optical fibers and retain comparable sensing performance. Based on this property, different materials can also be loaded on the surface of the optical fiber for remote detection of other analytes. It is expected to facilitate the research on fiber-optic-based integrated biosensors and show application prospects in diverse fields such as biochemical analysis and disease diagnosis.

1. Introduction

Quantitative detection of biological components has received much attention in various fields, especially biomedicine and food-related fields (Xue et al., 2019). During the detection, biological samples with pathogenic microorganisms such as bacteria and viruses may bring safety problems and even lead to the infection of the operators, which places more demands on remote detection. Remote detection offers the possibility of spatial separation of the operators from the sample to be detect, which would effectively interrupt the transmission of pathogenic microorganisms in the sample (Modesti et al., 2020). In recent years, as the prevalence of SARS-COVID-19 rises, research on remote biosensors has attracted more and more attention. For example, biosensors based on fluorescence analysis have been proposed for remote identification of six species of bacteria (Nissler et al., 2020). Biosensors based on electrochemical analysis were developed for the remote detection of urea (Kuo et al., 2021).

Among the various analysis methods, photoelectrochemical (PEC) analysis has numerous advantages, such as high sensitivity, quick response and anti-interference (Bott et al., 2021; Mazzaracchio et al., 2022). Therefore, it is irreplaceable in comparison with many other analysis methods. In this method, the light is usually applied as an excitation source to generate photoelectrons and holes in the conduction band and valence band of the semiconductor material, respectively. The redox reaction between electrons or holes and the analyte will cause a change of the current, so the concentration of the analyte can be obtained by analyzing the current. However, due to the large-volume spatial light, studies on remote biosensors based on the PEC analysis method are very limited. On the other hand, optical fiber sensors have the advantages of tiny size, low loss, and strong anti-interference ability, which make them widely used in aerospace, civil engineering, biomedicine, and other fields (Yu et al., 2019; Thomas et al., 2021). In particular, optical fiber exhibits excellent biocompatibility (Guo et al., 2016; Zhao et al., 2019; Du et al., 2020), so it has a minimal impact on the biological activity of the sample. Therefore, an integrated PEC biosensor can be constructed by loading conductive media and other materials on the surface of the optical fiber. The fiber-optic-based PEC biosensor can not only provide the possibility for remote detection but also simplify the optical path and dramatically improves the integration of the detection device.

On the other hand, cysteine (Cys) is a common amino acid with a unique sulfhydryl structure, and it has been used in health products and food additives (Wu et al., 2021). Cysteine has optical isomerism and can be divided into L-cysteine and D-cysteine. In living organisms, cysteine exists in the L configuration. L-cysteine is the precursor of protein, and also participates in the synthesis of metabolites such as glutathione and taurine (Yin et al., 2016). For the human body, Cys has the function of maintaining the redox balance of the nervous system, and its abnormal content may lead to some diseases, such as Alzheimer's disease and Parkinson's disease (Gonzalez et al., 2018). Cys is present not only in human serum but also in human urine. (Tiwari et al., 2016). The detection of Cys in urine samples have major implications for the screening and early diagnosis of such kidney disease (Li et al., 2022). According to Ref. (Siener et al., 2021), urinary cysteine levels of healthy people were 29.0 ± 17.0 μM in mixed diet and 25.1 ± 17.7 μM in vegetarian diet. However, urinary cysteine level in kidney disease disorders was 300 ± 168 μM (Ivanov et al., 2017). For the detection of Cys, researchers have developed analysis methods such as colorimetric fluorescence (Ma et al., 2022), Raman spectroscopy (Pei et al., 2022), electrochemical (EC)

analysis (Zhang et al., 2018), and photoelectrochemical (PEC) analysis (Yang et al., 2021). Some groups also proposed various biosensors.

In this paper, an integrated PEC Cys biosensor with remote detection function is proposed. The biosensor has a linear range of 0.01~1 µM with a low LOD of 3.17 nM. In the device, an optical fiber probe loaded with ITO/ZnO/Cu$_2$O acts not only as the working electrode of the biosensor, but also as an optical waveguide to replace the large-volume spatial light. Among them, ITO as a transparent conductive material, can not only transmit electrons but also has excellent optical transmittance. Cu$_2$O is a P-type semiconductor and combines to Cys through Cu-S bonds. ZnO is a typical N-type semiconductor (Xia et al., 2014) and forms a heterostructure with Cu$_2$O to facilitate electrons and hole separation. The biosensor was compared with conventional PEC biosensors based on spatial light and demonstrated rapid detection of Cys in synthetic urine samples. Moreover, remote detection tests at a distance of 100 m were also performed. The fiber-optic-based PEC biosensor shows excellent potential in designing and fabricating integrated and remote biosensing systems.
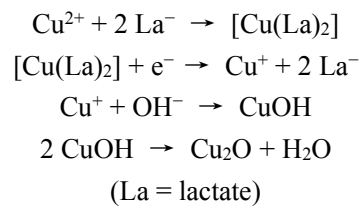
2. Material and methods

2.1. Construction of the sensing system and the design of sensing devices

In this design, ZnO/Cu$_2$O was modified on the surface of ITO glass and ITO deposited optical fiber. Properties of the sensing systems based on spatial light and the integrated optical fiber path were compared. Fig. 1A is the PEC sensing system based on ITO/ZnO/Cu$_2$O glass photoelectrode. The glass photoelectrode, platinum foil and Ag/AgCl electrode act as the working electrode (WE), counter electrode (CE), and reference electrode (RE), respectively. During the detection, the ITO/ZnO/Cu$_2$O glass photoelectrode was irradiated by spatial light (Ceaulight CEL-HXFUV300-T3 xenon lamp, 150 mW/cm^2). Fig. 1B shows an integrated PEC sensing system based on the optical fiber loaded with ITO/ZnO/Cu$_2$O. The modified optical fiber probe was used as the WE, and the detection of Cys was achieved through an optical fiber path. Compared to the glass photoelectrode in Fig. 1A, the optical fiber probe in Fig. 1B not only acts as a WE to react with the analyte but also directs the light exactly where it is needed.

The in-situ preparation of the electrode material is shown in Fig. 1C and 1D. Before this, the optical fiber was first pretreated. The polymer coating of the optical fiber (Yangtze HP200/230) at one end was removed by an optical fiber clamp. Then, the exposed quartz optical fiber was wiped with ethanol. To construct a conducting layer without affecting the light transmission, ITO is deposited on the surface of the optical fiber. The ITO layer was fabricated by magnetron sputtering deposition with an ITO target. In this procedure, the gas pressure was controlled at 9×10^{-4} Pa, and the discharge voltage was applied for 16 min at 20 V. Subsequently, the in-situ electrochemical deposition of ZnO was carried out on the surface of the ITO. The electrolyte solution was an aqueous solution with 5 mM Zn(NO$_3$)$_2$ and 10 mM CH$_3$COONH$_4$. During the deposition, heating in a 70 °C water bath with magnetic stirring and a constant potential of -1.2 V vs. Ag/AgCl were applied for 30 min. After that, in-situ electrochemical deposition of Cu$_2$O was also performed on ITO/ZnO electrode materials. The electrolyte solution was an aqueous solution with 50 mM CuSO$_4$ and 0.1 M L-lactic acid. The pH of the solution was adjusted with 4 M NaOH. The electrolytic solution was heated in a 40 °C water bath with magnetic stirring, and deposited at

a constant potential of -0.4 V vs. Ag/AgCl for 30 min. The possible reaction mechanism is as follows:
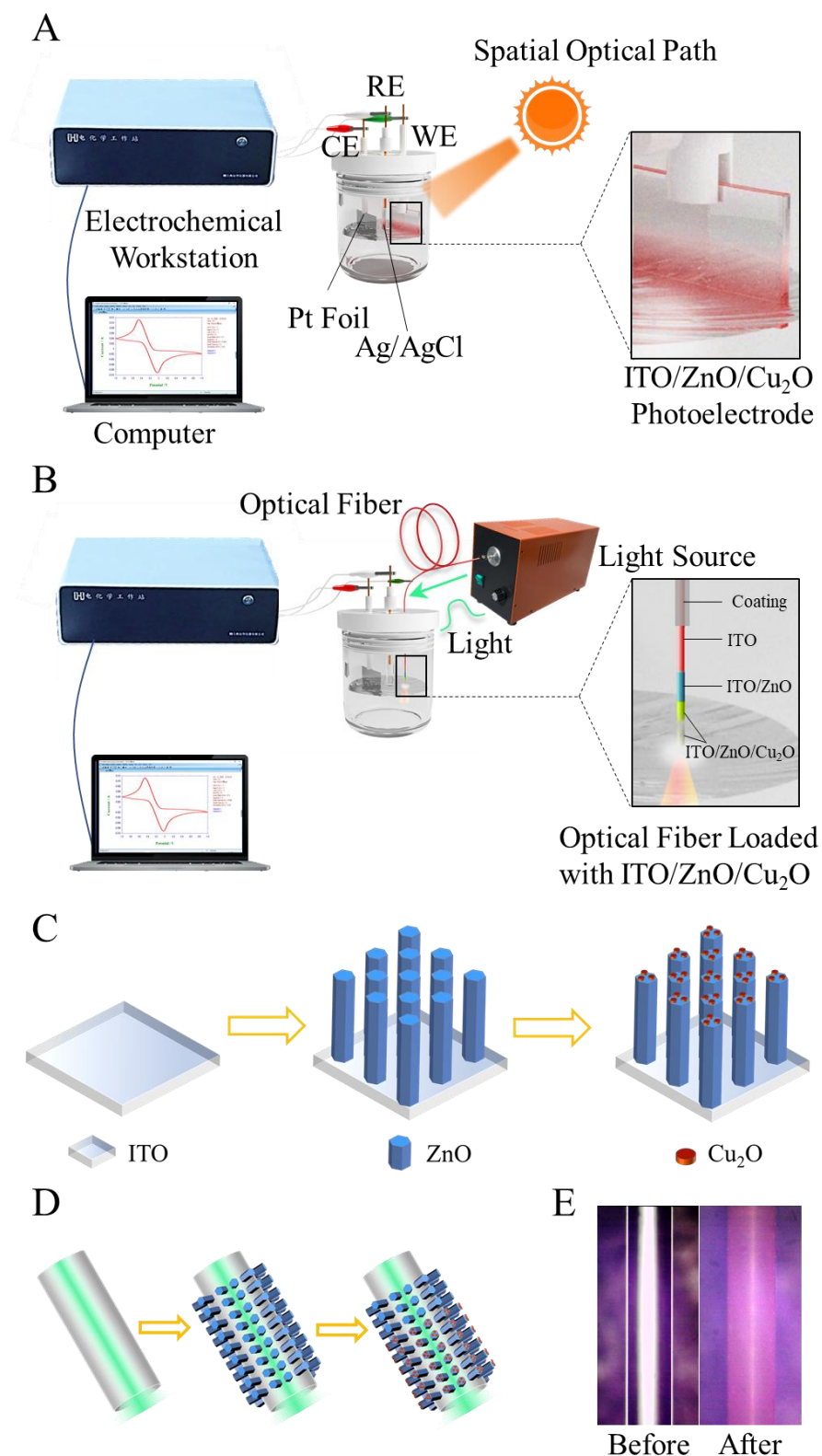
$$Cu^{2+} + 2\ La^- \rightarrow [Cu(La)_2]$$

$$[Cu(La)_2] + e^- \rightarrow Cu^+ + 2\ La^-$$

$$Cu^+ + OH^- \rightarrow CuOH$$

$$2\ CuOH \rightarrow Cu_2O + H_2O$$

$$(La = lactate)$$

Fig. 1. Schematic illustration of the two sensing devices and preparation of the electrode material. (A) The PEC biosensor based on ITO/ZnO/Cu$_2$O glass photoelectrode. (B) The PEC biosensor based on the optical fiber loaded with ITO/ZnO/Cu$_2$O. (C) Schematic illustration of the preparation process of the electrode material in the glass photoelectrode. (D) Schematic illustration of the preparation process of the electrode material in the optical fiber probe. (E) Optical micrographs of the optical fibers before and after electrochemical deposition. The diameter of the optical fibers is 200 μm.

Fig. 1E presents the optical micrographs of the fabricated optical fibers before and after electrochemical deposition. The results show that the morphology of optical fiber surface changes significantly before and after the modification. This implies that the conductive and sensing layers are uniformly attached to the surface of the optical fiber after the modification. During the detection process, the excitation light in the optical fiber can act on the electrode material through scattering and subsequently excite the photoelectrons to transmit along the ITO conductive layer.

2.2. Structure characterization and the performance of modified sensor devices

The microscopic morphologies of glass photoelectrodes and optical fiber probes were investigated by field emission scanning electron microscope (FESEM, ZEISS Gemini 500). The elemental composition of the $ITO/ZnO/Cu_2O$ optical fiber probe was examined by energy dispersive X-Ray spectroscopy (EDS, Bruker Xflash 6130). X-ray diffractometer (XRD, Rigaku TTR-IIIB) and X-ray photoelectron spectroscopy (XPS, Thermo Fisher, Escalab Xi+) were used to analyze the crystal structure and chemical state. Electrochemical impedance spectroscopy (EIS) of the glass photoelectrode and the optical fiber probe were studied in 0.1 M KCl aqueous solution. Cyclic voltammetry (CV) and square wave voltammetry (SWV) tests were carried out in 0.1 M KCl aqueous solution with Cys. The photocurrent measurement of the glass photoelectrode and the optical fiber probe used a xenon lamp and optical fiber-coupled tungsten halogen light (Ocean Optics LS-300) as light sources, respectively. All analytes were dissolved in 0.1 M phosphate buffered saline (PBS) with a pH of 7.4. PBS is an aqueous solution with KH_2PO_4, Na_2HPO_4, KCl and NaCl. All aqueous solutions were prepared using deionized water with a resistivity of 18.25 MΩ·m. Furthermore, the detection of Cys in synthetic urine was performed by the standard addition method. The synthetic urine contained urea, sodium citrate, oxalic acid, Na^+, K^+, NH_4^+, Ca^{2+}, Mg^{2+}, Cl^-, $H_2PO_4^-$, and SO_4^{2-}, etc. Before the detection, KH_2PO_4 and Na_2HPO_4 were added to the synthetic urine to provide buffer capacity. For remote detection tests, the Cys capsules (Grandpharma) were dissolved in PBS and centrifuged at 8000 r/min for 3 min, and the resulting supernatant was taken as another real sample for detection.

3. Results and Discussion

3.1. Chemical Characterization of Electrode Material

Scanning electron microscopy (SEM) was used to study the surface morphologies of glass photoelectrodes and optical fiber probes. The SEM images of the ITO/ZnO glass photoelectrode, the $ITO/ZnO/Cu_2O$ glass photoelectrode, the ITO/ZnO optical fiber probe and the $ITO/ZnO/Cu_2O$ optical fiber probe are given in Fig. 2A~D. Among them, ZnO has a hexagonal prism shape, and the size of ZnO on the surface of optical fiber is smaller than the size of ITO glass. The morphologies of Cu_2O are in the form of nanosheets that cover the surface of ZnO. In comparison, on the surface of optical fiber, more Cu_2O nanosheets were obtained, and the morphology of ZnO was also more intact, thus indicating a larger contact area between the two materials. Surface analysis of the $ITO/ZnO/Cu_2O$ optical fiber probe is shown in Fig. 2E. In the image, the optical fiber probe is placed horizontally in the middle of the field of view. It can be seen that the surface of the optical fiber was uniformly covered by electrode materials. Moreover, to investigate the

elemental distribution on the surface of the optical fiber probe in Fig. 2E, the EDS mapping was further measured in detail as shown in Fig. 2F~H. It can be seen that O, Zn, and Cu elements are homogeneously distributed on the surface of the optical fiber. The background contains more Cu elements due to the presence of the copper sheet as a background.
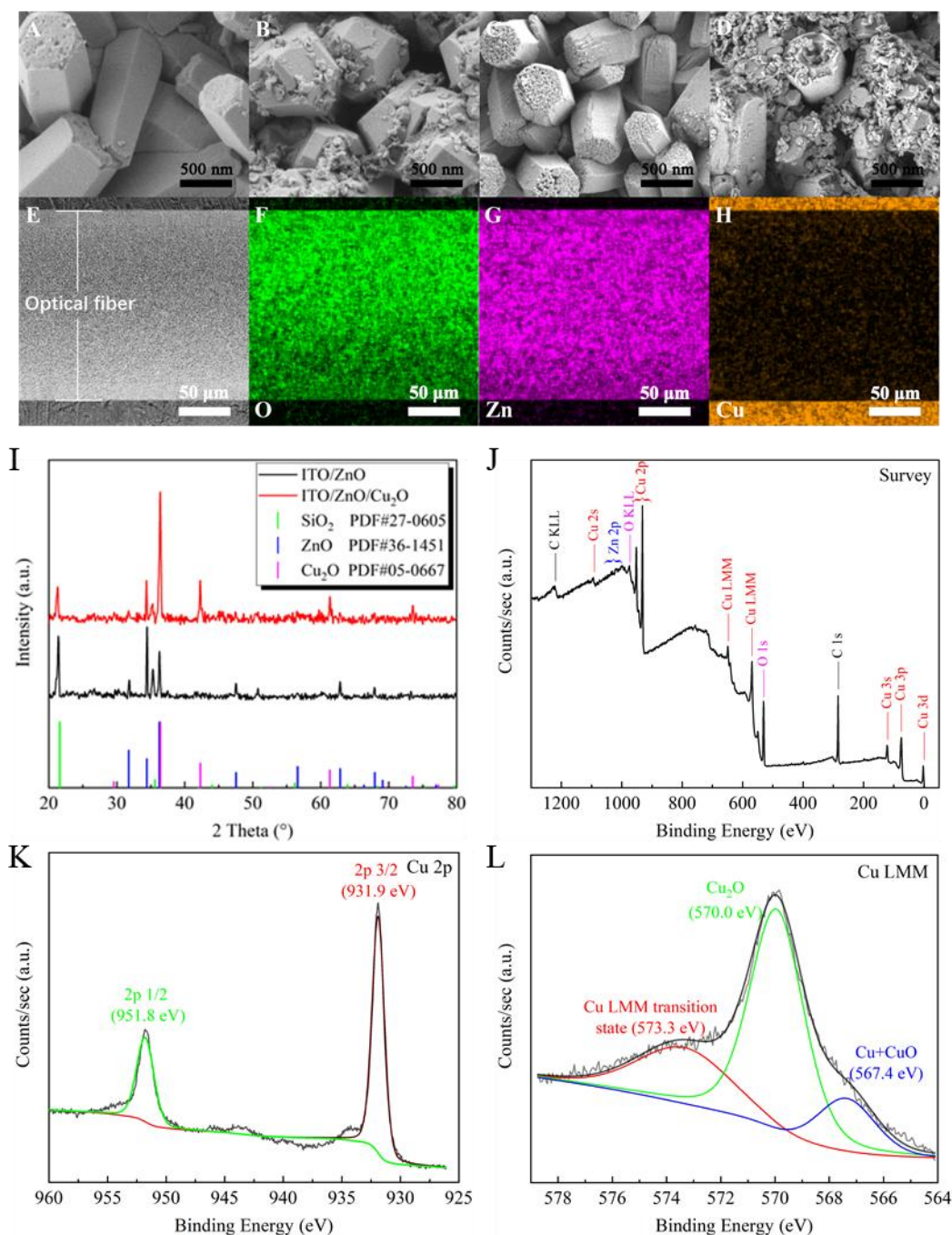

Fig. 2. Chemical characterization of glass photoelectrodes and optical fiber probes. (A) SEM images of the ITO/ZnO glass photoelectrode. (B) SEM images of the ITO/ZnO/Cu$_2$O glass photoelectrode. (C) SEM images of the ITO/ZnO optical fiber probe. (D) SEM images of the ITO/ZnO/Cu$_2$O optical fiber probe. (E) Topography of the surface of the ITO/ZnO/Cu$_2$O optical fiber probe. (F) The elemental mapping of O element. (G) The elemental mapping of Zn element. (H) The elemental mapping of Cu element. (I) Multiplot of XRD spectra of ITO/ZnO glass photoelectrode and ITO/ZnO/Cu$_2$O glass photoelectrode. (J) XPS survey spectrum of ITO/ZnO/Cu$_2$O glass photoelectrode. (K) High-resolution XPS spectrum of Cu 2p. (L) LMM Auger electron energy spectrum of Cu.

However, the chemical composition and oxidation states of the electrode materials still need further analysis since EDS mapping can only determine the elemental composition. Therefore, XRD was applied to characterize the glass photoelectrode with more nanomaterials. Fig. 2I presents the XRD patterns of the ITO/ZnO glass photoelectrode and the ITO/ZnO/Cu$_2$O glass photoelectrode. In this figure, the two curves have eight diffraction peaks in common. Among these, the diffraction peaks at 21.6, 35.62 and 51.22° are generated by the substrate SiO$_2$. The diffraction peaks at 31.77, 34.42, 36.25, 62.86, and 67.96° have been assigned to the (100), (002), (101), (103), and (112) crystal planes of the typical tetrahedron ZnO with PDF number of 36-1451 (Tian et al., 2019; Jian et al., 2021), respectively. In the XRD pattern of ITO/ZnO/Cu$_2$O, three new diffraction peaks appeared at 42.30, 61.34, and 73.53°, which are related to the (200), (220), and (311) crystal planes of cubic Cu$_2$O with PDF number of 05-0667 (Alhumaimess et al., 2020), respectively. In addition, due to the overlap of the diffraction peak of Cu$_2$O at 36.41° and that of ZnO at 36.25°, the peak intensity of ITO/ZnO/Cu$_2$O here is significantly higher than that of ITO/ZnO.

XPS spectrum has been acquired to further explore the chemical states of ITO/ZnO/Cu$_2$O composite material, as shown in Fig. 2J, which confirms the existence of Cu, Zn, and O elements. In comparison, the Zn peak is weaker than the Cu peak, which means that the content of Zn element on the surface of the electrode is lower than that of Cu element. Further, the high-resolution XPS spectrum of Cu 2p is shown in Fig. 2K. It can be seen that two signature peaks of Cu 2p 1/2 and Cu 2p 3/2 at 951.8 and 931.9 eV consistent with Ref. (Jing et al. 2019). However, the XPS spectra of Cu 2p peaks of Cu, Cu$^+$, and Cu^{2+} have similar binding energy, so it is difficult to determine the valence state of Cu (Sun et al., 2018). Therefore, the LMM Auger electron energy spectrum of Cu is given in Fig. 2L. In particular, the strong peak at 570.0 eV confirms that most Cu atoms are present in the form of Cu$_2$O. However, due to the inability to completely isolate the air, a small amount of Cu$_2$O is oxidized, resulting in the production of Cu and CuO with a small peak at 567.4 eV. The above EDS, XRD, and XPS results together indicate the successful preparation of ZnO and Cu$_2$O.

3.2. Electrochemical Characterization

To study the electrochemical behavior of Cys on the ITO/ZnO/Cu$_2$O electrode system, CV and SWV tests were performed in the range of 0~1 V and 0~0.5 V, respectively. Fig. 3A shows the CV curves for different scan rates. It can be seen that each curve has only one oxidation peak around 0.3 V but no reduction peak, which suggests that in the potential range of 0~1 V, only the oxidation reaction from cysteine to cystine occurs. In addition, a significant positive correlation between the anodic peak current (i_{pa}) and the scan rate was observed. To better visualize the relationship, Fig. 3B shows the linear relationship between i_{pa} and the square root of the sweep rate. Similarly, the SWV curve given in Fig. 3C, i_{pa} shows a positive correlation with frequency. Fig. 3D shows i_{pa} versus the square root of the frequency. Both linear relations indicate that the electrochemical behavior of Cys on the surface of the electrode is dominated by diffusion-control and follows Faraday's law. In other words, the following quantitative detection of Cys can be achieved by electrochemical methods.
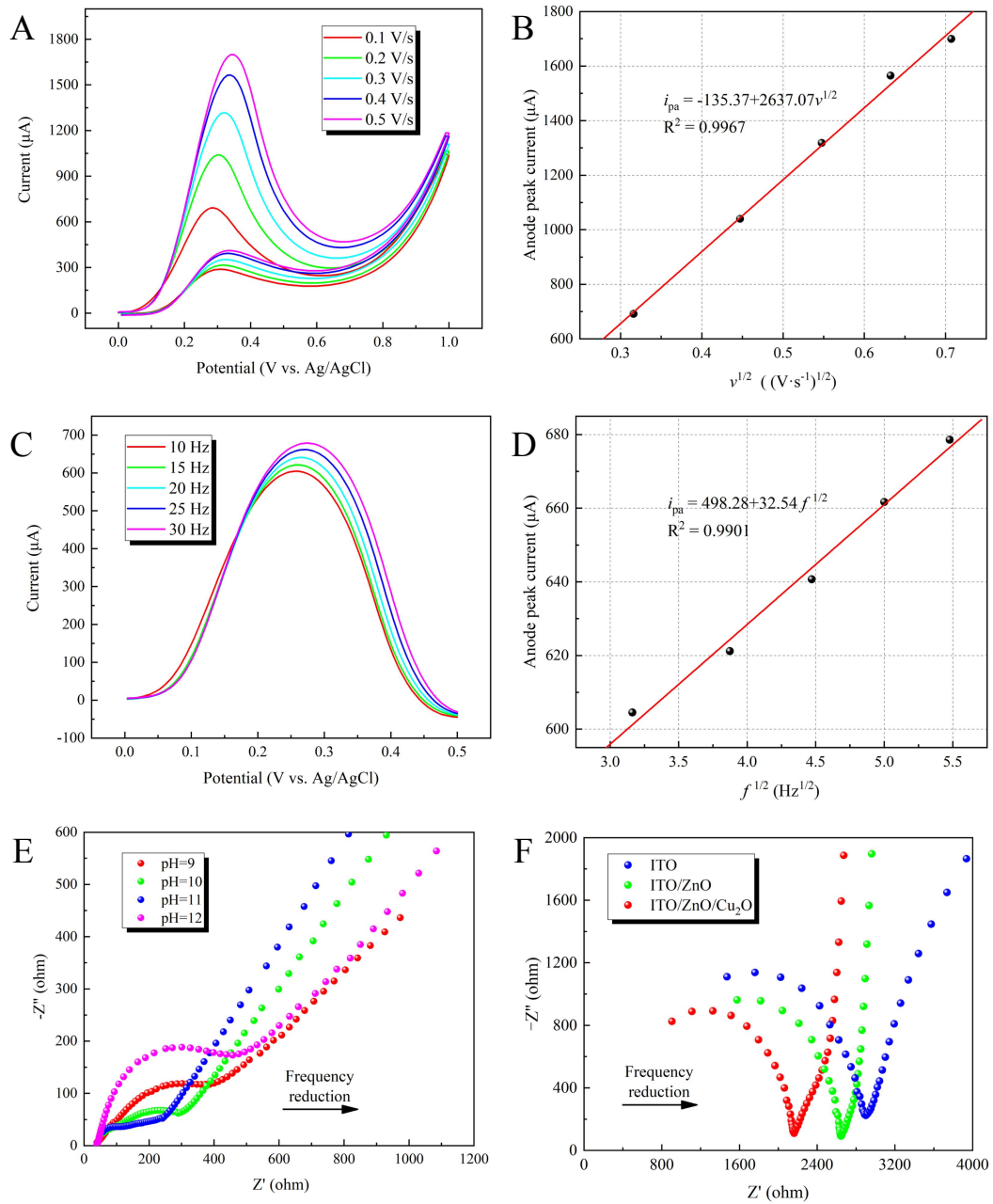
Fig. 3. CV and SWV curves of Cys of KCl solution and Nyquist plots under different conditions. (A) CV curves for different scan rates. (B) Anodic peak current versus square root of scan rate. (C) SWV curves for different frequencies. (D) Anodic peak current versus square root of frequency. (E) The Nyquist plots of Cu_2O prepared in solutions of different pH. (F) The Nyquist plots of the optical fiber loaded with different electrode materials.

In addition, during the preparation of Cu_2O, the pH of the electrolyte solution affects the electrochemical performance of the photoelectrode, and this effect was investigated by EIS. The Nyquist plots of Cu_2O prepared in solutions of different pH (9,10,11,12) are shown in Fig. 3E. In the Nyquist plots, the high-frequency region generally includes an incomplete semicircle. Its diameter reflects the interfacial resistance between the electrode and the solution which is mainly the charge transfer resistance (CTR) (Li et al., 2019). An inclined straight line in the low-frequency region represents the Warburg impedance, and a higher slope of the line suggests

faster ion diffusion (Kou et al., 2019). Each Nyquist plot contains the incomplete semicircle and the inclined straight line constitutes. According to Fig. 3E, the Cu$_2$O prepared at pH 11 has the smallest diameter of the incomplete semicircle in the high-frequency region and the largest slope in the low-frequency region, indicating that the photoelectrode prepared at pH 11 has the smallest charge transfer resistance and the fastest ion diffusion. Therefore, the photoelectrode prepared at pH 11 has better electrochemical performance.

For the optical fiber probe loaded with different electrode materials, their EIS have also been studied, as shown in Fig. 3F. It can be seen that the slope of the low-frequency region in the Nyquist plot increases significantly after the modification of ZnO on the surface of the optical fiber. Then, after the loading of Cu$_2$O, the diameter of the incomplete semicircle in the high-frequency region is significantly reduced. This implies that the charge transfer ability of the optical fiber is enhanced, and the ion diffusion speed is accelerated. There are two possible explanations for the improvement of electrochemical performance. On the one hand, the two nanomaterials provide a larger specific surface area, improving the contact area between the electrode and the solution will be improved. On the other hand, the PN junction formed by the two electrode materials causes the directional migration of the carriers. The two together lead to the result.
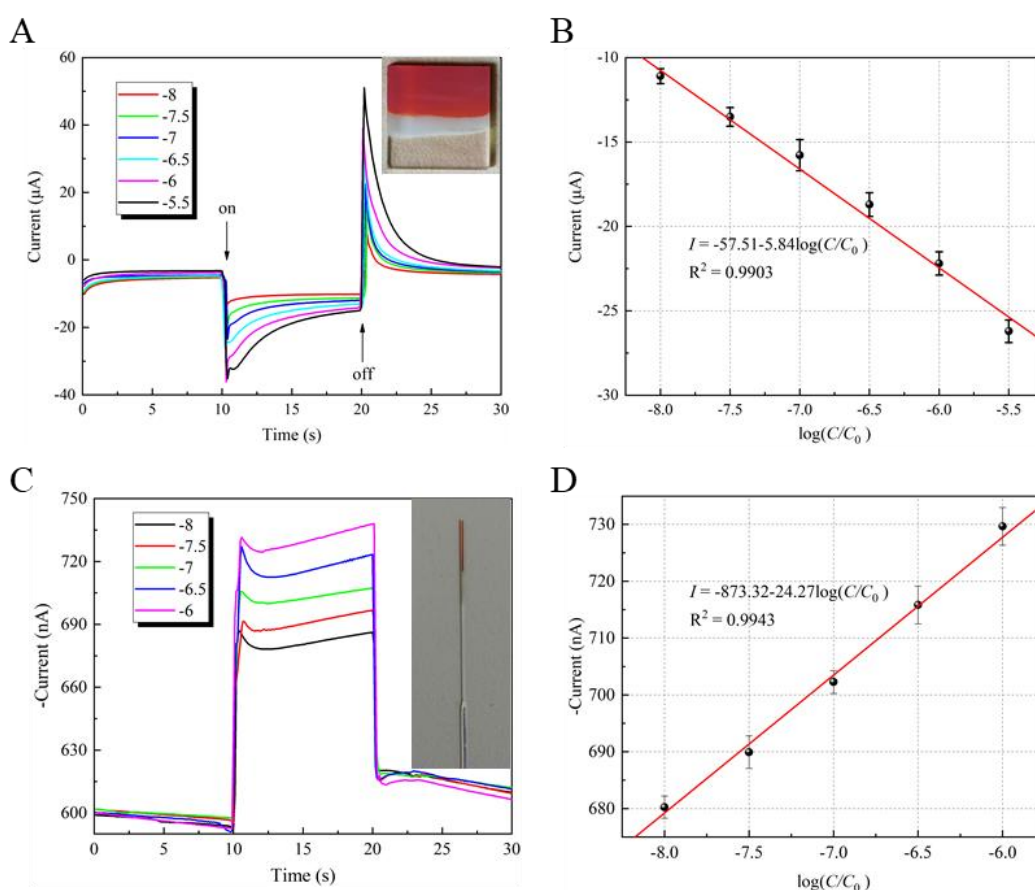

Fig. 4. Photocurrent curves. (A) Current of the PEC biosensor base on glass photoelectrode in PBS with different concentrations of Cys. Inset: Physical photograph of the ITO/ZnO/Cu$_2$O glass photoelectrode. (B) Linear regression of photocurrent versus concentration in (A). (C) Currents of the fiber-optic-based PEC biosensors in PBS with different concentrations of Cys. Inset: Physical photograph of the ITO/ZnO/Cu$_2$O optical fiber probe. (D) Linear regression of photocurrent versus concentration in (C). Error bars indicate standard deviations, n = 3.

3.3. Performance of the PEC Biosensors

Most PEC sensors establish a relationship between photocurrent and analyte concentration. Fig. 4A shows the current responses of the PEC biosensors based on ITO/ZnO/Cu$_2$O glass photoelectrode in PBS with different concentrations of Cys. Under detection, the light source was turned on at 10 s, resulting in a negative photocurrent. The negative photocurrent gradually increased with the increase of Cys concentration. After 10 s, the light source was turned off, and a forward current generated at this time due to the free electrons in the PN junction returning to the ground state. Taking the photocurrent at 12 s as an example, the linear relationship between the photocurrent (I) and the logarithm of the Cys concentration ($\log C/C_0$) is given in the range of 10^{-8} M to $10^{-5.5}$ M, as shown in Fig. 4B. Therefore, the PEC biosensor based on ITO/ZnO/Cu$_2$O photoelectrode shows a linear range of 0.01 μM to 3.16 μM with regression coefficient (R^2) value of 0.9903.

Likewise, the photocurrents were measured at a bias potential of 0 V by the fiber-optic-based integrated PEC biosensor, and the results are shown in Fig. 4C. Similarly, the negative photocurrent increases with the increase of Cys concentration. Fig. 4D also shows the linear regression between the photocurrent and the logarithm of the Cys concentration in the range of 0.01 μM to 1 μM. The integrated PEC biosensor achieved a limit of detection (LOD) of 3.17 nM with a higher R^2 value of 0.9943. The calculation of LOD is according to Ref. (Li et al., 2021). The slight decrease in the linear range may be caused by the decrease in the electrode area. According to the error bars in Fig. 4D, the integrated PEC biosensor still maintains a high accuracy. In addition, when the light source is turned off, no significant reverse current is generated, and the current quickly returns to a steady state.
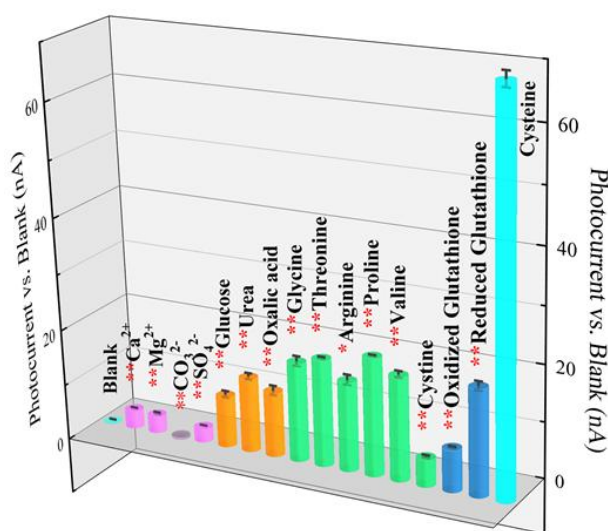

Fig. 5. Specificity of the fiber-optic-based PEC biosensors for Cys. Error bars indicate standard deviations, n = 3. Statistical significance was tested using a 1-tailed paired samples t-test. *: P < 0.01; **: P < 0.001.

Specificity is a critical index for the performance of biosensors. In order to evaluate the specificity of the fiber-optic-based PEC biosensor, photocurrent detection was performed on 100 μM several interfering substances, and 1 μM Cys, respectively. The detection was performed in PBS. Since the PBS contains relatively high concentration of Na$^+$, K$^+$, Cl$^-$, H$_2$PO$_4^-$, HPO$_4^{2-}$, etc.,

slight changes in the concentration of these ions are not believed to interfere with the biosensor. To make the results more intuitive, the photocurrent of the blank sample (PBS without Cys) is used as a benchmark. In this experiment, each sample was measured three times and the error bars were given. The results are shown in Fig. 5. It can be seen that the addition of CO_3^{2-} leads to a slight decrease in the photocurrent, while the addition of other interfering ions leads to a slight increase. Among them, simple organics and amino acids have a greater impact than inorganic ions. This is due to the presence of high concentration inorganic ions in the PBS, which make the addition of inorganic ions hardly changes the conductivity of the liquid to be detected. For cystine and oxidized glutathione, the interference ability is limited due to the absence of sulfhydryl groups in their molecular structures. The molecular structure of reduced glutathione contains a sulfhydryl group, but its molecule is larger and has a greater steric hindrance. It means that the sulfhydryl groups are harder to combine to the electrode material. Therefore, reduced glutathione is more difficult to oxidize than Cys, which causes only a small change in photocurrent.

In Fig. 5, 100 μM interfering substances can cause a photocurrent change of 20.90 nA at most, while only 1 μM Cys can cause a change of 69.08 nA. Moreover, the P-values of the measured results was calculated by a 1-tailed paired samples t-test (Karmakar et al., 2015). The P-values of each interfering substances were less than 0.01. It suggests that there is a statistically significant difference between each interfering substances and analyte. This fully demonstrates that the sensor has high specificity to Cys. The reason is that the sulfhydryl group of Cys is easy to combine with the Cu atom in the electrode material Cu_2O. Under the illumination, Cys is oxidized by holes in Cu_2O, which results in a significant change in current. The detailed analysis will be provided in section 3.4. In addition, common substances in human urine such as inorganic ions and urea have little interference with Cys detection. Therefore, the integrated PEC biosensor has the ability to detect Cys in urine.

Table 1. Quantitative detection of Cys in spiked synthetic urine.

Sample	Added (nM)	Photocurrent (nA)	Found (nM)	Recovery (%)
1	0	686.7	20.4	/
	100	705.7	124.0	103.60
2	0	687.5	22.1	/
	200	711.7	219.2	98.55
3	0	686.4	19.9	/
	300	716.0	329.6	103.23

The applicability of the biosensor was verified by experiments. Since the composition of real urine varies from person to person, the synthetic urine was used as one real sample. By the standard addition method, 0.1, 0.2 and 0.3 μM Cys were added into the synthetic urine, respectively. The photocurrents before and after addition were detected by the integrated PEC biosensor, and calculated recoveries were 98.55~103.60%, as shown in Table 1. Therefore, the proposed integrated biosensor has the ability to detect real samples. Furthermore, based on the optical fiber coupling and the computer remote control technology, Cys capsules were taken as another real sample and detected by the fiber-optic-based PEC biosensor at a distance of 100 m.

The results are shown in Table 2. Moreover, a comparative study of this work with the existing Cys biosensor is performed in Table 3.

Table 2. Remote detection of Cys in real samples (N=5).

Standard concentration (μM)	Photocurrent (nA)	Detected concentration (μM)	Measurement error (%)
1.000	727.4	0.972	2.80
1.000	728.6	1.089	8.90
1.000	727.6	0.990	1.00
1.000	726.8	0.918	8.20
1.000	727.1	0.944	5.60

Table 3. A comparative study of this work with the existing Cys biosensor.

Method	Material	pH	Linear range (μM)	R^2 value	References
Fluorescent	Fluorescent probe	7.4	0~80	0.9956	Wang et al., 2017
Fluorescent	Fluorescent probe	7.4	0~10	/	Fu et al., 2017
EC	Y_2O_3-NPs/N-rGO	7.0	1.3~720	0.9951	Yang et al., 2016
EC	Pt-CNT	7.4	0.5~100	0.9991	Peng et al., 2018
PEC	metal-organic gel-derived CuO	/	0.1~0.6	0.995	Yang et al., 2021
PEC	ZnO/Cu_2O	7.4	0.01~3.16	0.9903	This work
Integrated PEC	ZnO/Cu_2O	7.4	0.01~1	0.9943	This work

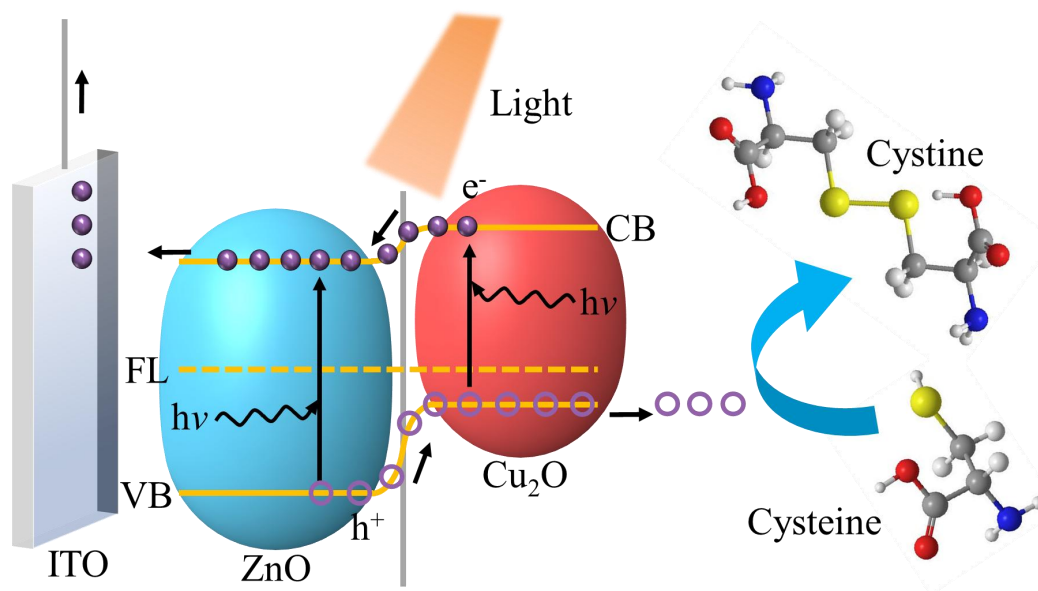NPs=nanoparticles, N-rGO= nitrogen-doped reduced graphene oxide, CNT=carbon nanotubes.

Fig. 6. Schematic illustration of the possible mechanism of the proposed PEC biosensor.

3.4. Possible Mechanism

A possible detection mechanism is presented as outlined in Fig. 6, which is equally applicable to the fiber-optic-based PEC biosensor. Under irradiation, if the energy of the photon is larger than the band gap of the semiconductor, the electrons in the valence band will be excited and transitioned to the conduction band to become free electrons. At the same time, holes are left in the valence band. ZnO is an N-type semiconductor, Cu_2O is a P-type semiconductor, and a PN junction forms near the interface between the two. In the absence of an external electric field, there is a gradient difference in the concentration of free electrons and holes in the PN junction. The two will spontaneously generate a diffusion effect and eventually reach equilibrium, forming a built-in electric field (Selopal et al., 2020). The drift effect caused by the external electric field can break the balance of the built-in electric field. Therefore, free electrons move from Cu_2O to ZnO, and holes move from ZnO to Cu_2O. As a result, a large number of holes accumulate in the valence band of Cu_2O. These holes can oxidize Cys in the solution to Cystine. As the reaction proceeds, more holes in Cu_2O are consumed. This is equivalent to new electrons entering the valence band of Cu_2O. These electrons are also excited by light, become free electrons, and enter the circuit. This process is ultimately reflected in the increase of the photocurrent. The photocurrent enhancement effect increases with the increase of Cys concentration. Since the reaction of Cys on the electrode surface is dominated by diffusion-control and follows Faraday's law, a linear relationship between Cys concentration and photocurrent is established. Unfortunately, the sulfhydryl groups of L-cysteine and D-cysteine both can be oxidized by holes, so the propose biosensor has not able to discriminate them.

4. Conclusions

An integrated biosensor for Cys has been proposed by modifying ITO, ZnO, and Cu_2O on the surface of the optical fiber. The optical fiber has the ability to conduct electricity and light, and electrode materials on the surface of the optical fiber can also interact with the analytes. The proposed integrated biosensor has a linear range of 0.01 μM to 1 μM, a low LOD of 3.17 nM and a high R^2 value of 0.9943, while exhibiting high selectivity and accuracy. The LOD is lower than the urinary Cys levels of healthy people and kidney patients so the proposed biosensor meets the detection requirement. The detection of Cys in spiked synthetic urine was realized by the integrated biosensor with recoveries of 98.55~103.60%. Moreover, the remote detection capability of the biosensor is demonstrated by the detection of real samples at a distance of 100 m. A fly in the ointment is that Cu_2O is prone to be oxidized, so the optical fiber loaded with ITO/ZnO/Cu_2O is not suitable for long-term storage. The next step in the research program is to integrate the sample cell into a microfluidic chip, which will further simplify the sensing device and hopefully help build a wearable biosensor.

References

Alhumaimess, M. S., Essawy, A. A., Kamel, M. M., Alsohaimi, I. H., Hassan, H. M. A., 2020. Nanomaterials 10, 781.

Bott-Neto, J. L., Martins, T. S., Buscaglia, L. A., Santiago, P. V. B., Fernandez, P. S., Machado, S. A. S., Oliveira, O. N., 2021. Sensor. Actuat. B Chem. 345, 130390.

Du, M., Huang, L., Zheng, J., Xi, Y., Dai, Y., Zhang, W., Yan, W., Tao, G., Qiu, J., So, K. F., 2020. Adv. Sci. 7, 2001410.

Fu, Z., Han, X., Shao, Y., Fang, J., Zhang, Z., Wang, Y., Peng, Y., 2017. Anal. Chem. 89,1937–1944.

Gonzalez, A. N. B., Vicentini, F., Calvo, D. J., 2018. J. Neurochem. 144, 50–57.

Guo, T., Liu, F., Liang, X., Qiu, X., Huang, Y., Xie, C., Xu, P., Mao, W., Guan, B., Albert, J., 2016. Biosens. Bioelectron. 78, 221–228.

Ivanov, A. V., Bulgakova, P. O., Virus, E. D., Kruglova, M. P., Alexandrin, V. V., Gadieva, V. A., Luzyanin, B. P., Kushlinskii, N. E., Fedoseev, A. N., Kubatiev, A. A., 2017. Electrophoresis 38, 2646–2653.

Jiang, Z., Sun, W., Miao, W., Yuan, Z. Yang, G., Kong, F., Yan, T., Chen, J., Huang, B., An, C., 2019. Adv. Sci. 6, 1900289.

Karmakar, S., Harcourt, E. M., Hewings, D. S., Lovejoy, A. F., Kurtz, D. M., Ehrenschwender, T., Barandun, L. J., Roost, C., Alizadeh, A. A., Kool, E. T., 2015. Nat. Chem. 7, 752–758.

Kou, W., Li, X., Liu, Y., Zhang, X., Yang, S., Jiang, X., He, G., Dai, Y., Zhen, W., Yu, G., 2019. ACS Nano 13, 5900–5909.

Kuo, P., Dong, Z., Chen, Y., 2021. IEEE T. Instrum. Meas. 70, 4004613.

Li, R., Zhou, X., Shen, H., Yang, M., Li, C., 2019. ACS Nano 13, 10049–10061.

Li, X., Qin, Z., Fu, H., Li, T., Peng, R., Li, Z., Rini, J. M., Liu, X., 2021. Biosens. Bioelectron. 177, 112672.

Li, Y., Liu, G., Ji, D., He, Y., Chen, Q., Zhang, F., Liu, Q., 2022. Analyst 147, 1403–1409.

Ma, Y., Mei, H., Li, Y., Zhou, P., Mao, G., Wang, H., Wang, X., 2022. Food Chem. 379, 132155.

Mazzaracchio, V., Marrone, R., Forchetta, M., Sabuzi, F., Galloni, P., Wang, M., Nazligul, A., Choy, K. L., Arduini, F., Moscone, D., 2022. Electrochim. Acta 426, 140766.

Modesti, P. A., Wang, J., Damasceno, A., Agyemang, C., Van, B. L., Persu, A., Zhao, D., Jarraya, F., Marzotti, I., Bamoshmoosh, M., 2020. BMC Med. 18, 256.

Nissler, R., Bader, O., Dohmen, M., Walter, S. G., Noll, C., Selvaggio, G., Gross, U., Kruss, S., 2020. Nat. Commun. 11, 5995.

Pei, J., Sun, Y., Yu, X., Tian, Z., Zhang, S., Wei, S., Zhao, Y., Boukherroub, R., 2022. J. Colloid Interf. Sci. 626, 608–618.

Peng, J., Huang, Q., Zhuge, W., Liu, Y., Zhang, C., Yang, W., Xiang, G., 2018. Biosens. Bioelectron. 106, 212–218.

Selopal, G. S., Mohammadnezhad, M., Besteiro, L. V., Cavuslar, O., Liu, J., Zhang, H., Navarro-Pardo, F., Liu, G., Wang, M., Durmusoglu, E. G., 2020. Adv. Sci. 7, 2001864.

Siener, R., Bitterlich, N., Birwe, H., Hesse, A., 2021. Nutrients 13, 528.

Sun, J., Yu, J., Ma, Q., Meng, F., Wei, X., Sun, Y., Tsubaki, N., 2018. Sci. Adv. 4, eaau3275.

Thomas, N., Singh, V., Kuss, S., 2021. Trac-Trend. Anal. Chem. 136, 116196.

Tian, H., Liu, X., Dong, L., Ren, X., Liu, H., Price, C. A. H., Li, Y., Wang, G., Yang, Q., Liu, J., 2019. Adv. Sci. 6, 1900807.

Tiwari, J., Vij, V., Kemp, K. C., Kim, K. S., 2016. ACS Nano 10, 46–80.

Wang, P., Wang, Q., Huang, J., Li, N., Gu, Y., 2017. Biosens. Bioelectron. 92, 583–588.

Wu, X., Guo, X., Zhu, K., 2021. Foods 10, 1156.

Xia, L., Song, J., Xu, R., Liu, D., Dong, B., Xu, L., Song, H., 2014. Biosens. Bioelectron. 59, 350–357.

Xue, J., Wu, T., Dai, Y., Xia, Y., 2019. Chem. Rev. 119, 5298–5415.

Yang, C., Wu, Q., Jiang, Z., Wang, X., Huang, C., Li, Y., 2021. Talanta 228, 122261.

Yang, S., Li, G., Wang, Y., Wang, G., Qu, L., 2016. Microchim. Acta 183, 1351–1357.

Yin, J., Ren, W., Yang, G., Duan, J., Huang, X., Fang, R., Li, C., Li, T., Yin, Y., Hou, Y., Kim, S. W., Wu, G., 2016. Mol. Nutr. Food Res. 60, 134–146.

Yu, S., Ding, L., Lin, H., Wu, W., Huang, J., 2019. Biosens. Bioelectron. 146, 111760.

Zhang, X., Sun, J., Liu, J., Xu, H., Dong, B., Sun, X., Zhang, T., Xu, S., Xu, L., Bai, X., Zhang, S., Mintova, S., Lu, G., Song, H., 2018. Sensor. Actuat. B Chem. 255, 2919–2926.

Zhao, Y., Tong, R., Xia, F., Peng, Y., 2019. Biosens. Bioelectron. 142, 111505.